analytical chemistry

Article

pubs.acs.org/ac

# A Comparison of Atomistic and Continuum Approaches to the Study of Bonding Dynamics in Electrocatalysis: Microcantilever Stress and *in Situ* EXAFS Observations of Platinum Bond Expansion Due to Oxygen Adsorption during the Oxygen Reduction Reaction

Evan M. Erickson,[†] Muhammed E. Oruc,[‡] David J. Wetzel,[†] Michael W. Cason,[†] Thao T. H. Hoang,[†] Matthew W. Small,[†] Diya Li,[§] Anatoly I. Frenkel,*[,∥] Andrew A. Gewirth,*[,†] and Ralph G. Nuzzo*[,†]

[†]Department of Chemistry, University of Illinois, Urbana, Illinois 61801, United States

[‡]Department of Chemical and Biomolecular Engineering, University of Illinois, Urbana, Illinois 61801, United States

[§]Department of Chemical and Biomolecular Engineering, University of Pennsylvania, Philadelphia, Pennsylvania 19104, United States

[∥]Physics Department, Yeshiva University, New York, New York 10016, United States

Supporting Information

**ABSTRACT:** Microcantilever stress measurements are examined to contrast and compare their attributes with those from *in situ* X-ray absorption spectroscopy to elucidate bonding dynamics during the oxygen reduction reaction (ORR) on a Pt catalyst. The present work explores multiple atomistic catalyst properties that notably include features of the Pt−Pt bonding and changes in bond strains that occur upon exposure to $O_2$ in the electrochemical environment. The alteration of the Pt electronic and physical structures due to $O_2$ exposure occurs over a wide potential range (1.2 to 0.4 V vs normal hydrogen electrode), a range spanning potentials where Pt catalyzes the ORR to those where Pt-oxide forms and all ORR activity ceases. We show that Pt−Pt surface bond strains due to oxygen interactions with Pt−Pt bonds are discernible at macroscopic scales in cantilever-based bending measurements of Pt thin films under $O_2$ and Ar. Complementary extended X-ray absorption fine structure (EXAFS) measurements of nanoscale Pt clusters supported on carbon provide an estimate of the magnitude and direction of the *in-operando* bond strains. The data show that under $O_2$ the M−M bonds elongate as compared to an $N_2$ atmosphere across a broad range of potentials and ORR rates, an interfacial bond expansion that falls within a range of 0.23 (±0.15)% to 0.40 (±0.20)%. The EXAFS-measured Pt−Pt bond strains correspond to a stress thickness and magnitude that is well matched to the predictions of a mechanics mode applied to experimentally determined data obtained via the cantilever bending method. The data provide new quantitative understandings of bonding dynamics that will need to be considered in theoretical treatments of ORR catalysis and substantiate the subpicometer resolution of electrochemically mediated bond strains detected on the macroscale.

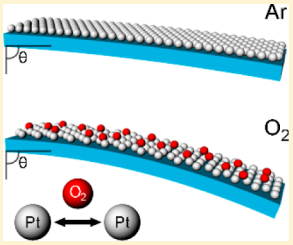


Platinum is a superior catalyst for the oxygen reduction reaction (ORR), but its high cost presents a major barrier to the commercial viability of technologies, such as polymer electrolyte membrane fuel cells, that require it.[1] The ORR has a large overpotential (ca. 0.4 V) in these cells, and high mass loadings are often needed to provide useful rates.[2,3] While work in finding non-noble-metal-based catalysts has led to considerable advances,[4−7] Platinum group metal (PGM) electrocatalysts remain the best ORR catalysts to date and notable for utilizing the high efficiency, direct four-electron reduction pathway.[8−10] An increase in Pt mass activity through increased surface area has lowered overall catalyst cost considerably, but edge effects reduce ORR site-specific activity in PGM catalysts, resulting in a nanoparticle size vs activity limit at 3−4 nm.[1,3,11−14] Alloying techniques can further maximize active surface area by exposing a larger ratio of the more active Pt (111) plane and also affect the electronic character of the catalyst.[10,15−21]

Catalytic activity balances on interrelated properties such as *d*-band occupancy, Pt−O bond strengths and distances, and $O_2$ adsorption activation barriers.[22−31] In particular, the *d*-band model, relating the energy difference between the d-band center and the Fermi level to the binding energy of the adsorbates, has been successfully applied to catalyst design.[32,33] These studies, both *ab initio* and experimental, have focused on the Pt−O bond, while presuming a static Pt−Pt bond character during ORR.[22−31] However, it is understood that there are significant reasons, and data,[34,35] that suggest such static models are too simplistic and a need exists for better information as to the real nature of the bonding dynamics.

There exist means that can be used, in principle, to measure such effects. Electrochemical surface stress measurements have long been used to investigate the lattice strain effects that result

**Received:** May 22, 2014
**Accepted:** July 28, 2014
**Published:** July 28, 2014

from electrodeposition, and the technique has recently been applied to the study of oxygen reduction.[36,37] Previously, Heaton and Friesen studied the stress-potential behavior of Pt and Au electrodes using electrocapillarity. More specifically, they described features in the surface stress behavior of Pt in oxygen saturated environments as they related to the onset of oxygen reduction.[38] Seo and Serizawa investigated the changes in surface stress of Pt electrodes in acidic and alkaline sulfate and alkaline fluoride solutions by a bending-beam method, one similar to the one we employ here.[39] Stafford et al. utilized a dynamic stress analysis, probing the capacitive response of Pt films in order to further understand the surface charge effects in the double layer region and the multiple stress generating effects caused by adsorbate interactions with the Pt surface.[40]

The present work addresses and compares quantitative measurement protocols that provide insights into the *in-operando* structural dynamics of electrocatalysts, using the ORR, carried out using a Pt catalyst, as an exemplary model system. Of specific concern in this work is the critical comparison of an *in situ* local probe of atomistic structure, X-ray absorption spectroscopy (XAS), and a continuum-level/macroscopic probe of interfacial dynamics, cantilever strain measurements, that embed these same atomistic features within the more macroscopic characteristics of the mechanics involved. The question addressed is the degree to which fully quantitative analyses of the atomistic features of the dynamics of electrocatalysis can be derived from such data.

*In situ* electrochemical surface stress measurements on Pt films track the macroscopic tensile and compressive responses (Figure 1a) to applied potentials under inert gas and $O_2$ sparged environments. In principle, this measurement can report on the Pt−Pt bond length change as a function of $O_2$ exposure, albeit at the macroscopic level. The mechanics are more complex than this, however, and other features of the interfaces involved can be (and are expected to be) important contributors to measured strain data.

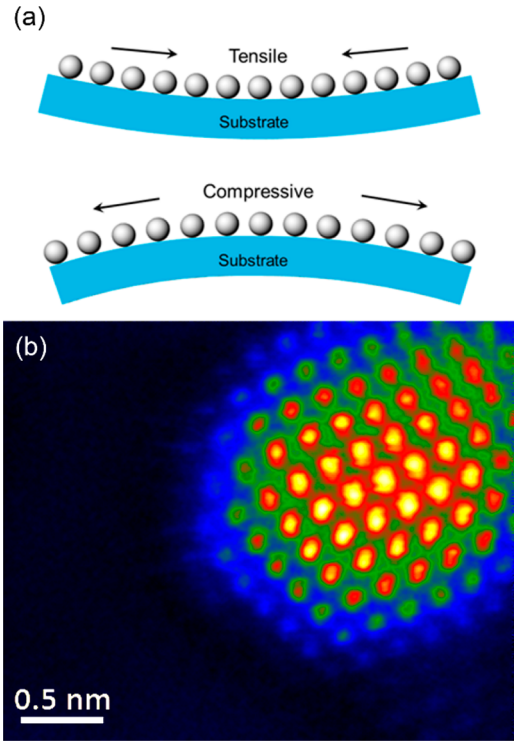


**Figure 1.** (a) The contraction or expansion of surface bonds yielding stresses that by convention are described as mediating either tensile or compressive modes of deflection in a macroscale cantilever, respectively. (b) Aberration-corrected STEM image of an exemplary, individual Pt nanoparticle supported on carbon.

XAS is a direct atomistic probe that provides an experimental method for measuring *d*-band model properties directly.[41−48] In an earlier report, *in situ* XAS studies of the ORR showed that the platinum catalyst oxidation state changes significantly with potential.[43,44] More recent *in situ* XAS studies of the ORR on Pt, ones benefiting from advances in XAS instrumentation and *in situ* cell designs, have made it possible to extend these insights and to quantitatively study more complex phenomena such as platinum oxide growth and potential-dependent bond disorder that results from perturbations due to interfacial bonding.[44,49,50] Our previous work used *in situ* electrochemical X-ray absorption near-edge structure (E-chem XANES) to show that the electronic structure of a Pt electrocatalyst is strongly influenced when exposed to $O_2$ under potentiostatic control, exhibiting larger *d*-band vacancies than exist at the same potential under $N_2$.[51] Additionally, the largest difference between the $O_2$ and $N_2$ integrated $\Delta\mu$(E) $L_3$-edge XANES data occurs at cathodic potentials. The change in $\Delta\mu$ between $O_2$ and $N_2$ exposure is associated with charge transfer between the Pt and the oxygen adsorbate. These results, obtained using 3 nm Pt nanoparticles, have been reproduced on the 1.2 nm particles used in the present work (*vide infra*). Figure 1b shows an atomic resolution scanning transmission electron microscopy (STEM) micrograph of a typical Pt/C supported nanoparticle in the 1.2 nm size range, comprised of Pt atoms well described by a truncated cuboctahedral shape.

A particular consequence of the charge transfer process—developed in our XANES work and in other studies referenced above—is that Pt−Pt bond distances should also exhibit dependences due to the $O_2$ exposure and potential. The nature of these structural changes have yet to be fully characterized—their study being complicated by the fact that they are likely to be local to the surface atoms of a supported electrocatalytic metal cluster. As the EXAFS reports on ensemble averages, the surface bonding information will be convolved with the more-bulk-like atomic bonding that is also present in a cluster. Very small clusters, however, can be used to more heavily weight (and thus better detect) changes due to surface bonding—dynamic bond strains that may be small and thus challenging to characterize *in operando*. It therefore remains an opportunity for progress in research to establish how bonding dynamics evolve quantitatively during the electrocatalysis of the ORR by Pt. The current work addresses this interest.

In this study, we explore the complementary attributes of two independent means through which bond strains manifested in an *in-operando* electrochemical environment can be explored. We specifically highlight the similarities that exist between macroscale mechanical stresses manifested in thin film cantilever measurements and the atomic-scale structural perturbations evidenced by EXAFS measurements made on small supported electrocatalytic Pt clusters—specifically, the surface localized bond strains evidenced in each system in the presence of $O_2$. The measurements reported in the current work demonstrate that these electrochemically mediated bond strains are in fact small, being manifested as an expansion that varies weakly over the range of potentials investigated. We demonstrate that the EXAFS and cantilever measurements (when analyzed via a suitable model) agree in terms of relative


dx.doi.org/10.1021/ac5019149 | *Anal. Chem.* 2014, 86, 8368−8375

magnitude and direction of the Pt−Pt bond strain (expansion) evidenced under $O_2$ during the ORR. Of particular note is the finding that the cantilever-based measurement reveals the nature of a generally weak potential dependence of the Pt−Pt bond strains with a higher analytical certainty.

## EXPERIMENTAL SECTION

In-situ stress data were collected using an optical stress measurement setup and cell described previously[52,53] while the electrochemistry was monitored with a CV-27 potentiostat (BASi West Lafayette, IN). Surface stress was measured using cantilever curvature as previously described[54,55] and was calculated using Stoney's equation.[56] Cyclic voltammetry was conducted using a modified glass coverslip as the working electrode, a Pt wire counter electrode, and a Ag/AgCl reference electrode. Cyclic voltammograms were measured at room temperature in Ar or $O_2$ saturated 0.1 M $HClO_4$ at a scan rate of 10 $mVs^{-1}$ from 1.6 to 0.0 V versus the normal hydrogen electrode (NHE). We note that the scan rate used is sufficiently low to ensure the stress response is reflective of a steady state regime, as further affirmed by estimates of the same as are predicted by the Cottrell equation.[57] Both the surface stress changes and the electrochemical data were recorded using a home-built program written using LabVIEW (National Instruments, Austin, TX).

Glass coverslips coated on one side with a 20 nm Ti adhesion layer and 200 nm of Pt were prepared from borosilicate glass microscope coverslips (Gold Seal No. 1, 150 $\mu$m thick, Young's modulus = 75.9 GPa). Cantilever-electrodes approximately 25 mm × 1.5 mm were then cut from the coverslips using a diamond-tipped pen in accordance with cantilever dimensions for accurate stress values.[52] The cantilever-electrodes were rinsed with Milli-Q water (>18 MΩ $cm^{-1}$) and annealed with a $H_2$ flame prior to use.

The Pt/C electrocatalyst used in this study was prepared using the incipient wetness technique followed by heating under a $H_2$ atmosphere, as described in the Supporting Information. The particle size distribution, obtained by using STEM was 1.20 ± 0.60 nm (Figure S1). The catalyst loading on the gas diffusion electrode was measured against a standard using X-ray micro tomography (MicroCT; Figure S2). The particle size distribution (1.23 ± 0.37 nm) and catalyst loading of the electrode were measured following XAS data acquisition and are given in the Supporting Information, showing the electrode and catalyst structures changed little during data acquisition (Figures S3 and S4).

The electrochemical *in situ* XAS cell featured oxygen permeable poly(dimethylsiloxane) windows as described previously.[51] Electrochemical measurements with the XAS cell were performed using a CH Instruments potentiostat. All potentials are referred (vs NHE), which was calibrated by exposing the Pt electrocatalyst to $H_2$ prior to experiments. The XAS experiments were obtained with the Pt catalyst operating in three potential regions: the double layer region, (400, 500, and 600 mV), at the onset potential for ORR (900 mV), and at a potential where the Pt is electrochemically oxidized to $PtO_x$ ($1 < x < 2$; 1200 mV). Electrochemical data for the XAS experiments can be found in the Supporting Information (Figure S5).

The XAS experiments were performed at the National Synchrotron Light Source at Brookhaven National Laboratory, beamline X18B. The beamline utilizes a Si (111) double-crystal monochromator, which was detuned 25% to minimize higher harmonics. Experiments were performed in fluorescence mode, using an Ar-filled Lytle detector for measuring fluorescence intensity from the sample. X-ray absorption through bulk Pt foil positioned downstream from the sample between the two Ar-filled ionization chambers was measured in the same energy scan with the electrochemical XAS data for energy calibration and alignment. Incident beam intensity was measured using a $N_2$-filled ionization chamber positioned upstream from the sample. Typical acquisition times were 20 min per scan with a typical potential point requiring up to 20 scans. Due to time constraints, only four XAS scans were performed at 1200 and 900 mV, which is the origin of the relatively large experimental uncertainties at these potentials compared to the data obtained at other potentials. EXAFS data were extracted from the raw absorption coefficient data using the Autobk method[58] implemented in the IFEFFIT data analysis package.[59] The data were Fourier transformed from k-space, where k is the photoelectron wavenumber, to R space and the fitting ranges for quantitative analysis in both k-space and R-space were determined. The data were fit in R-space with FEFF6 theory.[60] For analyzing the structural changes obtained at different potentials, only the nearest neighbor Pt−O and Pt−Pt contributions to EXAFS were included in the theory. Since EXAFS cannot distinguish between O and C as the scattering atom, "Pt−O" refers to any pair of Pt and O or C as the 1NN. For 3D structure determination of a representative particle from the ensemble, we applied a multiple scattering analysis method that takes into account five nearest Pt−Pt coordinations, including multiatom linkages, as described in greater detail below and in the Supporting Information.

## RESULTS AND DISCUSSION

**Electrochemical Stress Measurements.** Figure 2 shows representative results of macroscopic electrochemical stress measurements made on a thin film Pt electrocatalyst during the ORR. Figure 2a shows voltammetry (vs NHE) obtained from the polycrystalline Pt/glass cantilever in an Ar purged electrochemical stress cell showing oxygen evolution at 1.4 V, oxide stripping between 0.7 and 0.5 V, hydrogen associated features below 0.2 V, and oxide formation at 0.8 V during the anodic sweep.[61] The data in Figure 2b, obtained under $O_2$, show that the ORR is operative on this surface, with an onset of ca. 0.8 V. The voltammetry presented here agrees with previous reports.[62,63]

Figure 2c shows electrochemical surface stress-thickness changes occurring on the cathodic sweep with and without the presence of $O_2$. Absent $O_2$, the Pt surface exhibits three regions of activity as the potential becomes more negative from 1.5 V to ca. 0.1 V. First, the surface stress becomes more tensile as the potential is swept to more negative values. Second, the tensile slope increases between 0.8 and 0.1 V but abruptly becomes more compressive between 0.1 V and the negative potential limit of 0.0 V. The form of the potential-stress profile is consistent with the results of prior reports.[39] The tensile stress observed between 0.8 and 0.4 V is assigned to surface contraction resulting from oxygen removal during reduction of the surface oxide.[61] The surface stress remains tensile as surface potential becomes more negative (0.5 to 0.2 V), which has been explained in the past as being a consequence of the increasing surface charge density in the double layer region. In general, increasing surface charge results in more attractive interactions between surface atoms, which cause tensile stress.[64,65] Nevertheless, Stafford et al. showed that isolating


dx.doi.org/10.1021/ac5019149 | Anal. Chem. 2014, 86, 8368−8375

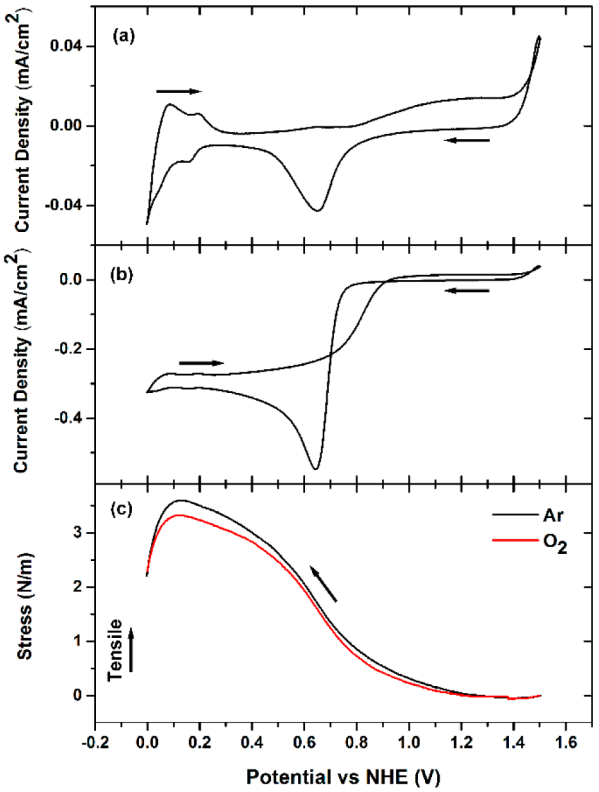


**Figure 2.** (a and b) Characteristic cyclic voltammograms of Pt/glass under Ar and $O_2$ sparged environments, respectively. (c) Stress data of Pt/glass of both Ar and $O_2$ conditions.

the contributions of adsorption using a macroscopic cantilever measurement, particularly within the double layer region, is not trivial.[40] Importantly, Figure 2c shows that while surface stress-thickness curves from Ar and $O_2$ saturated solutions exhibit similar patterns, the curve from the $O_2$-exposed sample is displaced in a more compressive direction over the entire potential window interrogated. The Δstress (Ar minus $O_2$) responses of Pt under $O_2$ and Ar behave as predicted by Feibelman's *ab initio* calculations, which predict a lengthening of M−M surface bonds that is a reduction in tensile surface stress of the Pt surface, in the presence of adsorbed oxygen.[66] As discussed in sections that follow, the quantitative aspects of these noted differences can be related to precise aspects of the M−M bonding dynamics, ones that EXAFS data help constrain and validate.

**EXAFS Data Modeling.** Data from XAS, here using small 1.2 nm average-sized clusters supported on C, help establish the magnitude of the structural relaxations that occur on Pt surfaces more similar to fuel cell catalysts, while simultaneously monitoring the electronic state of the d-band. The EXAFS region in XAS refers to the oscillatory part of the X-ray absorption coefficient that begins at about 40 eV past the absorption edge. The oscillations originate from the interference of the outgoing and backscattered photoelectron waves.[45,46] These fine structure oscillations are analyzed quantitatively by fitting a theoretical EXAFS equation that takes into account multiple scattering contributions of photoelectron paths,[60] to the experimental data. From such fits, the bond distances of the metal−metal and metal−adsorbate pairs, their coordination numbers, as well as the values of mean square bond length disorder, $\sigma^2$ can be obtained.[45,46]

Multiple scattering analysis of a representative nanoparticle sample, for the size/shape determination purpose, was performed using an approach reported in previous work.[67,68] Figure 3 depicts the EXAFS data in k-space (Figure 3a) and R-

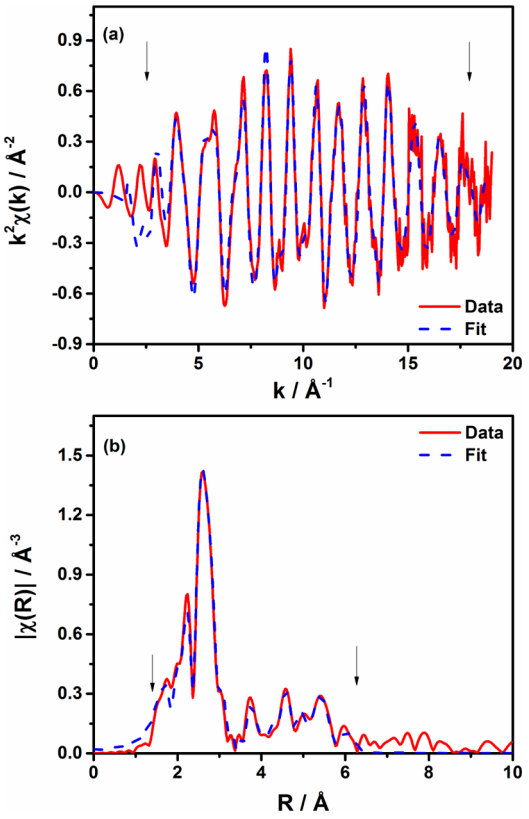


**Figure 3.** (a) k space and (b) R space plots of the $k^2$-weighted EXAFS data under $N_2$ at 400 mV, with a multiple-scattering fit. Best fit results or coordination numbers for Pt−Pt shells from 1 through 4 are presented in Table 1. The k-space and r-space Fourier transform window boundaries used for the fits are marked with black arrows.

space (Figure 3b) obtained with the sample held at a potential of 400 mV under $N_2$. The k-space range used in the Fourier transform was from 2.8 to 17.6 Å$^{-1}$, and the R-range used in the fit was from 1.4 to 6.3 Å. The k-space data obtained at other potentials are shown in Figure S6. The $k^2$-weighting was applied to all the data. The most prominent peak at ca. 2.6 Å, uncorrected for the photoelectron phase shift, is due to the Pt−Pt contribution. The fitting region in k-space and r-space are indicated by arrows. The fitting model included the Pt−O contribution for the first nearest neighbor to a Pt atom as well as Pt−Pt contributions corresponding to the first five nearest coordination spheres around Pt absorbers in the face centered structure. Multiple scattering paths were included in the theoretical calculation as well, as described in greater detail in the SI. The best fit results for the average coordination numbers of Pt−Pt neighbors in the coordination spheres of 1 through 4 around a Pt atom present in the cluster are presented in Table 1. The entire list of fit results is reported in Table S1 in the SI.

The electrochemical structural sensitivities at all potentials were analyzed for the nearest neighbor Pt−O and Pt−Pt contributions. The Pt−Pt bond distances obtained from EXAFS fits (Figure S7−S10) of the R-space data are plotted


dx.doi.org/10.1021/ac5019149 | *Anal. Chem.* 2014, 86, 8368−8375

Table 1. Coordination Numbers from EXAFS Derived Data from the Sample Measured under $N_2$ at 400 mv and the Mean Particle Diameter Obtained by STEM, Compared to Three Cuboctahedral Models

| | total atoms | $N_1$ | $N_2$ | $N_3$ | $N_4$ | diameter/nm |
|---|---|---|---|---|---|---|
| experiment | n/a | 6.7 ± 0.4 | 3.1 ± 1.5 | 12.3 ± 4.7 | 4.7 ± 1.4 | 1.2 ± 0.6 |
| models | 10 | 4.8 | 1.2 | 2.4 | 0.6 | 0.55 |
| | 37 | 7.0 | 2.4 | 7.1 | 3.2 | 1.1 |
| | 92 | 8.2 | 3.2 | 10.4 | 5.0 | 1.7 |

versus potential in Figure 4A. The figure shows an increase in Pt−Pt bond distance, $\langle R \rangle$, upon exposure to oxygen at all potentials relative to $N_2$. Figure 4B shows the average bond expansion, $\Delta\langle R \rangle$. It is defined as the difference between the average bond distances under $O_2$, $\langle R \rangle_{O_2}$, and $N_2$, $\langle R \rangle_{N_2}$, according to eq 1.

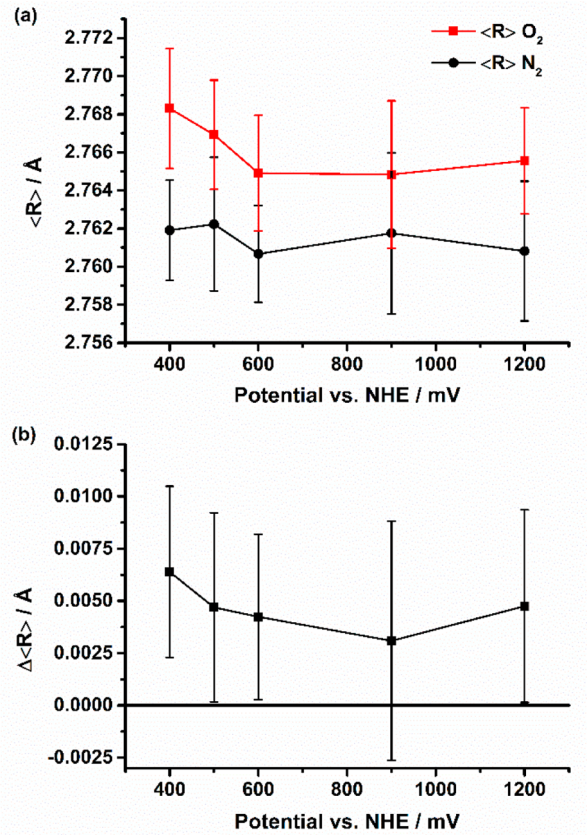


Figure 4. (a) Pt−Pt bond distances under $N_2$ and $O_2$ at three potentials in the double layer region (400 mV, 500 mV, and 600 mV) and at the ORR onset potential (900 mV) and at an oxidizing potential (1200 mV). (b) $\Delta\langle R \rangle$ at all potentials, showing a distinct expansion at all potentials upon exposure to $O_2$.

$$\Delta\langle R \rangle = \langle R \rangle_{O_2} - \langle R \rangle_{N_2} \quad (1)$$

Figure 4A shows that Pt−Pt distance under $O_2$ exposure is systematically longer compared to the $N_2$ exposure, despite a partial overlap of the Pt−Pt distance error bars at potentials greater than 500 mV. This expansion is more clearly observed in the differential potential-dependent distances $\Delta\langle R \rangle$ (Figure 4B). The trends seen here show that the $O_2$ environment, across a range of potentials that include the double layer region, leads to small, but measurable, bond length elongation. These modest trends are ones that are also inferred by mechanics models applied to the cantilever data, a point discussed below.

**Pt Nanoparticle Modeling.** The measured bond length expansion is intrinsically averaged over all bonds sampled in the EXAFS experiment. The bonds averaged include those on the surface and in the interior of the Pt nanoparticle. Surface relaxations figure very prominently for supported Pt clusters of this size. In order to estimate the surface contribution to the overall bond length expansion, we modeled the Pt nanoparticle by constructing it to be consistent with the EXAFS derived coordination numbers and STEM-determined size range as described below.[67]

In order to obtain the effective coordination number and thus particle size to estimate the surface contribution to the EXAFS, we utilized results of the multiple-scattering fit to the data, described above (Figure 3) and tabulated in Table 1. The relevant structural parameters for modeling the particle size and shape are the coordination numbers ranging from the first coordination shell ($N_1$) to the fourth ($N_4$). The coordination numbers and the STEM-determined average particle diameter (1.2 ± 0.6 nm, Figure S1) were compared against their respective theoretical values calculated for three models of the hemispherically truncated (with 111 plane) cuboctahedron (T-CO) series to determine the best size that fits both EXAFS and STEM sets of results. The T-CO nanoparticles are thought to be a good model for supported Pt nanoparticles at the length scale considered here.[67,69] Table 1 shows that the T-CO most closely related to the combination of the experimental data (EXAFS and STEM) is that of a 1.1 nm, 37 atom particle. This average cluster structure is depicted schematically in Figure 5. Figure S3 shows that minimal particle size changes occur during the course of the EXAFS measurement.

Figure 5 shows the cuboctahedral model used to define a surface-restricted expansion. In this surface-restricted model, the basal plane atoms are coordinated with the carbon support and are therefore considered static atoms (blue). Surface atoms are represented in green. There are 129 total bonds ($N_{total}$) in this model, 75 of which involve at least one surface atom

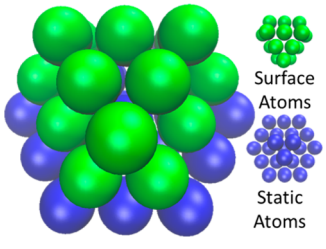


Figure 5. Depiction of the 37 atom, hemispherically truncated cuboctahedral nanoparticle, the best of the three models in terms of their agreement with EXAFS results (Table 1, Table S2). This T-CO was used for calculating the maximum, surface-restricted expansion. The static atoms in the surface-restricted expansion model (eq S5) are represented in blue, whereas the dynamic surface Pt atoms are represented in green. This ideal particle has 37 atoms with 129 total Pt−Pt bonds, of which 75 lengthen when the 15 surface atoms expand.


dx.doi.org/10.1021/ac5019149 | Anal. Chem. 2014, 86, 8368−8375

($N_{surface}$) and 54 of which involve only static atoms ($N_{static}$; Figure S11).

Using the 37 atom T-CO model, maximum and minimum values of the surface Pt−Pt bond expansion can be calculated from the ensemble-average EXAFS results; as the ORR is a surface phenomenon, it seems reasonable to assume that primarily the surface bonds will change during a reaction while the subsurface bonds and those surface bonds involving the carbon support will remain relatively unperturbed. Averaging over only the surface atoms results in the estimated maximum surface bond expansion value (*vide infra*). The opposite extreme is uniform bond expansion over the whole nanoparticle, resulting in the estimated minimum surface bond expansion value.

Figure 6 reports these minimum and maximum oxygen-induced expansion values as a function of potential, using the

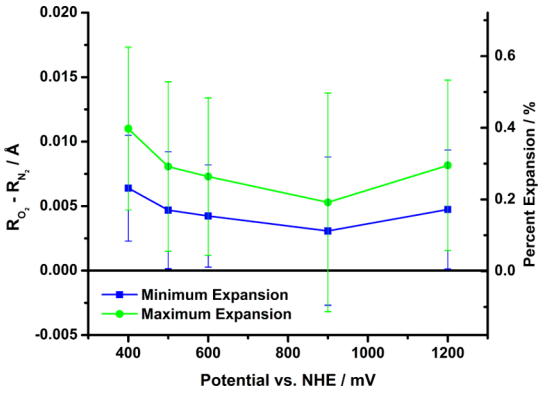


**Figure 6.** Minimum and maximum Pt−Pt surface bond expansion under $O_2$ calculated from the ensemble measurement and surface-restricted expansion. Plotted are both absolute expansions, $\Delta\langle R\rangle_{Min}$ and $\Delta\langle R\rangle_{Max}$, and percent expansion. Derivations are included in the Supporting Information.

modeling described above and in the Supporting Information (Figure S11). The figure shows there is a clear Pt−Pt surface bond expansion in the presence of $O_2$ at 400 mV, regardless of the model chosen. The expansion at this potential ranges from 0.006 (±0.004) Å for the ensemble minimum expansion to 0.011 (±0.006) Å for surface-restricted maximum expansion. These data correspond to 0.23 (±0.15)% to 0.40 (±0.2)% relative expansions of the Pt−Pt bonds under $O_2$ over the Pt−Pt bonds present under $N_2$. Figure 6 also shows the magnitudes of the Pt−Pt expansion occurring in the presence of $O_2$ at other more positive potentials using the same limiting cases of the model. These data and calculations are detailed in the Supporting Information (Table S3).

Adsorbate induced surface relaxation is a commonly observed phenomenon,[70−73] with lattice constant changes of about a few tenths of an Ångstrom being common for Pt.[74−77] For example, hydrogen adsorption has been shown to expand the Pt−Pt near-surface bonds by 0.05 Å or less.[78] Such values are important, and theoretical modeling suggests that the surface lattice constant is linearly related to the energy of the d-band center.[76] As the lattice expands, the d-band contracts, raising the energy of electrons near the Fermi level that can be donated to adsorbates. The XAS experiment probes both these bond length changes (via EXAFS) and the perturbations in the electronic structure (via XANES) in the same *in situ* experiment. To this end, we repeated the XANES white line intensity measurements performed on 3 nm Pt/C particles in previous work,[51] with the 1.2 nm Pt/C particles employed here, with similar trends being observed (Figures S12−S14). The increased potential-dependent ΔXANES intensify differences seen between $O_2$ and $N_2$ sparged environments, especially at more cathodic potentials, corresponds to an increase in electron density at or near the Fermi level and thus to an increase in the stability of $O_2$ and O adsorbates. At the same time, the unoccupied orbitals directly above the Fermi level are lowered in energy, reducing antibonding repulsion present in O adsorption.[76]

**Comparison of Cantilever and EXAFS Results.** The data in Figure 7 show the differences between potential-dependent

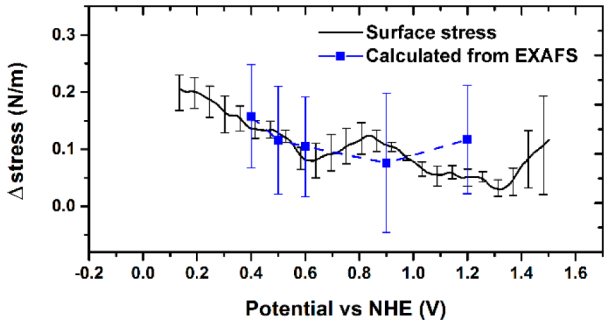


**Figure 7.** Characteristic stress differences obtained from *in situ* cantilever and EXAFS measurements. The black line shows delta stress of Ar minus $O_2$ (from Figure 2c), and the blue points indicate the expected delta stress based on the Pt−Pt bond strains obtained via EXAFS.

stress data for the Ar and $O_2$ cases more directly, with the $O_2$ displacement being evidenced lying between 0.05 and 0.2 N/m. Interestingly, we see in the cantilever measurement that the compressive displacement observed in the presence of $O_2$ is larger at more cathodic potentials. Though this trend appears to be in qualitative agreement with the increased Pt−Pt bond expansion found in the EXAFS measurements reported above, the magnitude of the errors in the EXAFS data given the exceedingly small bond length changes being measured make it impossible to state with certainty what the functional form of the potential dependence might be other than that it must be weak over the potential range examined.

In order to compare the relative magnitudes of Δstress observed in the two measurements, we next use the EXAFS-derived Pt−Pt bond expansion to calculate a limiting magnitude for a M−M bond stress in order to compare this value with experimental ones. In cantilever-based measurements the stress is calculated using Stoney's equation:[52]

$$\Delta\sigma = \sigma^{t} - \sigma^{0} = \frac{Y_s t_s^{2} C}{6(1-\nu_s)} \quad (2)$$

Here, $\Delta\sigma$ is the change in stress, $Y_s$ is the Young's modulus of the substrate, $t_s$ is the substrate thickness, $C$ is the curvature of the cantilever, and $\nu_s$ is the Poisson ratio of the substrate. Stoney's equation is valid in the limit where stress is proportional to the (elastic) strain via the Young's modulus of the material:[56]

$$\sigma_f = \epsilon_f Y_f \quad (3)$$

where $\sigma_f$ is the stress in the film, $\epsilon_f$ is the strain in the film, and $Y_f$ is the Young's modulus of the film. The Young's modulus for


dx.doi.org/10.1021/ac5019149 | Anal. Chem. 2014, 86, 8368−8375

Pt thin films has been reported in the literature to have some variation, typically having values slightly less than that of bulk Pt.[79,80] A value of 147 GPa was taken from the literature and used as a reasonable approximation for this calculation.[81]

The bond expansion is used to calculate the strain via:

$$\epsilon_f = \Delta D/a \quad (4)$$

where $\Delta D$ is the change in bond distance and $a$ is the Pt−Pt bond distance. From the 400 mV data from EXAFS, $\epsilon_f$ ranges between 0.0023 and 0.0040 (using the minimum and maximum expansion models described above). Assuming the stress to be manifested over one atomic layer, i.e. using data from the maximum expansion model, an estimated stress thickness can be calculated, as is reported in Figure 7.

Figure 7 shows the stress-thickness derived from the EXAFS measurements overlaid with the change in stress due to $O_2$ exposure obtained from the cantilever method. Strikingly, the EXAFS derived stress-thickness nearly exactly overlaps the data from the cantilever-based measurement. As the potential decreases, compressive stress increases in the oxygenated system. It is interesting to note that the uncertainties in the EXAFS measurement give rise to error bars in the stress calculation that are larger than those found with the cantilever method. The nearly quantitative agreement in magnitude between the two techniques nonetheless means that other putative sources of stress change upon $O_2$ exposure—such as defects, surface roughness, and impurities—are likely insignificant contributors in this case and that cantilever measurements, via atomistic models of the mechanics, can yield information relevant to bond dynamics manifested at subpicometer length scales.

## CONCLUSION

This work shows that adsorbed $O_2$ results in Pt−Pt bond expansion relative to Pt absent this gas. The Pt−Pt bond length increases at more negative potentials as oxides are removed from the Pt surface. Electrochemical surface stress measurements obtained from Pt films shows that the presence of $O_2$ leads to compressive stress relative to the $O_2$-free case, the magnitude of which is nearly identical to that predicted using the Pt−Pt bond expansion obtained from the EXAFS. Our observation of oxygen induced Pt−Pt bond expansion provides additional input for computational studies examining the dynamic Pt−Pt bond during the ORR. It is shown here that the underlying atomistic bond dynamics manifest in macroscopic, measurable stress changes in a benchtop, microcantilever experiment.

The current results suggest that cantilever-based surface stress measurements, when conjoined with mechanics modeling, can provide a simple and quantitative means through which one can explore surface-localized bond dynamics of metal electrocatalysts, doing so in ways that compliment *in-operando* data provided by XAS. We believe the current results suggest an important role that these methods can play in mechanistic studies of electrocatalysis. Our future work will explore this possibility, specifically for cases involving multimetallic compositions where more complex forms of atomistic dynamics may contribute to ORR catalytic activity.

## ASSOCIATED CONTENT

### Supporting Information

STEM micrograph and size distribution of the Pt nanoparticles before and after operation; MicroCT loading calculation of the electrodes before and after operation; k-space and R-space in $O_2$ and $N_2$ comparisons at each potential; EXAFS fits in k-space and R-space; detailed bond calculations of the model hemispherically truncated cuboctahedron; tabulated data of EXAFS derived values; XANES data and comparison to previous study, R-space comparison, electrochemical behavior during XAS data acquisition including cyclic voltammograms, chronoamperometric plots, and limiting current densities at different potentials, all in $N_2$ and $O_2$. Additional information pertaining to the maximum expansion model is also included. This material is available free of charge via the Internet at http://pubs.acs.org.

## AUTHOR INFORMATION

### Corresponding Authors

*E-mail: anatoly.frenkel@yu.edu.
*E-mail: agewirth@illinois.edu.
*E-mail: r-nuzzo@illinois.edu.

### Author Contributions

The manuscript was written through contributions of all authors. All authors have given approval to the final version of the manuscript.

### Funding

This work was primarily based on funding provided by the U.S. DOE (Grant DE-FG02-05ER46260). A.I.F. and R.G.N. acknowledge support by the U.S. DOE (Grant DE-FG02-03ER15476). Beamline X18B at the NSLS is supported in part by the Synchrotron Catalysis Consortium (U.S. DOE Grant DE-FG02-05ER15688). In addition, DL acknowledges support by the Catalysis Center for Energy Innovation, an Energy Frontier Research Center funded by the U.S. Department of Energy, Office of Science, Office of Basic Energy Sciences under Award Number DE-SC00010004.

### Notes

The authors declare no competing financial interest.

## ACKNOWLEDGMENTS

The authors thank Bluma Dukesz for her help during XAS data acquisition process. The work of Jim Brownfield and Derek Lutz in forming a functional flow box has been fundamental in our ability to carry-on this research. The authors thank Stoyan Bliznakov, Kotaro Sasaki, and the Adžić group for their help at BNL as well as Daniel Perlitz of UIUC for his contributions regarding thin film mechanics.

## ABBREVIATIONS

| | |
|---|---|
| NHE | normal hydrogen electrode |
| PGM | platinum group metals |
| ORR | oxygen reduction reaction |
| XAS | X-ray absorption spectroscopy |
| XANES | X-ray absorption near-edge structure |
| EXAFS | extended X-ray absorption fine structure |

## REFERENCES

(1) Gasteiger, H. A.; Kocha, S. S.; Sompalli, B.; Wagner, F. T. *Appl. Catal., B* **2005**, *56*, 9.
(2) Carrette, L.; Friedrich, K. A.; Stimming, U. *ChemPhysChem* **2000**, *1*, 162.
(3) Gewirth, A. A.; Thorum, M. S. *Inorg. Chem.* **2010**, *49*, 3557.
(4) Zhang, X.; Guo, J.; Guan, P.; Liu, C.; Huang, H.; Xue, F.; Dong, X.; Pennycook, S. J.; Chisholm, M. F. *Nat. Commun.* **2013**, *4*, 1924.
(5) Liu, R.; Wu, D.; Feng, X.; Müllen, K. *Angew. Chem., Int. Ed.* **2010**, *49*, 2565.

(6) Lee, J.-S.; Park, G. S.; Kim, S. T.; Liu, M.; Cho, J. *Angew. Chem., Int. Ed.* **2013**, *52*, 1026.
(7) Wang, S.; Yu, D.; Dai, L. *J. Am. Chem. Soc.* **2011**, *133*, 5182.
(8) Walch, S.; Dhanda, A.; Aryanpour, M.; Pitsch, H. *J. Phys. Chem. C* **2008**, *112*, 8464.
(9) Parthasarathy, A.; Martin, C. R.; Srinivasan, S. *J. Electrochem. Soc.* **1991**, *138*, 916.
(10) Wu, G.; More, K. L.; Johnston, C. M.; Zelenay, P. *Science* **2011**, *332*, 443.
(11) Mayrhofer, K. J. J.; Strmcnik, D.; Blizanac, B. B.; Stamenkovic, V.; Arenz, M.; Markovic, N. M. *Electrochim. Acta* **2008**, *53*, 3181.
(12) Adora, S.; Soldo-Olivier, Y.; Faure, R.; Durand, R.; Dartyge, E.; Baudelet, F. *J. Phys. Chem. B* **2001**, *105*, 10489.
(13) Ye, H.; Crooks, J. A.; Crooks, R. M. *Langmuir* **2007**, *23*, 11901.
(14) Tritsaris, G. A.; Greeley, J.; Rossmeisl, J.; Norskov, J. K. *Catal. Lett.* **2011**, *141*, 909.
(15) Moffat, T. P.; Mallett, J. J.; Hwang, S. *J. Electrochem. Soc.* **2009**, *156*, B238.
(16) Stamenkovic, V. R.; Fowler, B.; Mun, B. S.; Wang, G.; Ross, P. N.; Lucas, C. A.; Markovic, N. M. *Science* **2007**, *315*, 493.
(17) Wu, J.; Zhang, J.; Peng, Z.; Yang, S.; Wagner, F. T.; Yang, H. *J. Am. Chem. Soc.* **2010**, *132*, 4984.
(18) Zhang, J.; Yang, H.; Fang, J.; Zou, S. *Nano Lett.* **2010**, *10*, 638.
(19) Cochell, T.; Manthiram, A. *Langmuir* **2012**, *28*, 1579.
(20) Hasche, F.; Oezaslan, M.; Strasser, P. *J. Electrochem. Soc.* **2012**, *159*, B25.
(21) Oezaslan, M.; Hasche, F.; Strasser, P. *J. Electrochem. Soc.* **2012**, *159*, B394.
(22) Chen, Y.; Liang, Z.; Yang, F.; Liu, Y.; Chen, S. *J. Phys. Chem. C* **2011**, *115*, 24073.
(23) Greeley, J.; Stephens, I. E. L.; Bondarenko, A. S.; Johansson, T. P.; Hansen, H. A.; Jaramillo, T. F.; Rossmeisl, J.; Chorkendorff, I.; Norskov, J. K. *Nat. Chem.* **2009**, *1*, 552.
(24) Hwang, S. J.; Yoo, S. J.; Jang, S.; Lim, T.; Hong, S. A.; Kim, S. *J. Phys. Chem. C* **2011**, *115*, 2483.
(25) Lima, F. H. B.; Zhang, J.; Shao, M. H.; Sasaki, K.; Vukmirovic, M. B.; Ticianelli, E. A.; Adzic, R. R. *J. Phys. Chem. C* **2007**, *111*, 404.
(26) Lu, Y.; Gasteiger, H. A.; Shao-Horn, Y. *J. Am. Chem. Soc.* **2011**, *133*, 19048.
(27) Norskov, J. K.; Rossmeisl, J.; Logadottir, A.; Lindqvist, L.; Kitchin, J. R.; Bligaard, T.; Jonsson, H. *J. Phys. Chem. B* **2004**, *108*, 17886.
(28) Okamoto, Y.; Sugino, O. *J. Phys. Chem. C* **2010**, *114*, 4473.
(29) Rossmeisl, J.; Norskov, J. K. *Surf. Sci.* **2008**, *602*, 2337.
(30) Stamenkovic, V.; Mun, B. S.; Mayrhofer, K. J. J.; Ross, P. N.; Markovic, N. M.; Rossmeisl, J.; Greeley, J.; Norskov, J. K. *Angew. Chem., Int. Ed.* **2006**, *45*, 2897.
(31) Zhou, W.; Yang, X.; Vukmirovic, M. B.; Koel, B. E.; Jiao, J.; Peng, G.; Mavrikakis, M.; Adzic, R. R. *J. Am. Chem. Soc.* **2009**, *131*, 12755.
(32) Lee, K. R.; Jung, Y.; Woo, S. I. *ACS Comb. Sci.* **2012**, *14*, 10.
(33) Xin, H.; Holewinski, A.; Linic, S. *ACS Catal.* **2012**, *2*, 12.
(34) Amakawa, K.; Sun, L.; Guo, C.; Hävecker, M.; Kube, P.; Wachs, I. E.; Lwin, S.; Frenkel, A. I.; Patlolla, A.; Hermann, K.; Schlögl, R.; Trunschke, A. *Angew. Chem., Int. Ed.* **2013**, *52*, 13553.
(35) Paredis, K.; Ono, L. K.; Behafarid, F.; Zhang, Z.; Yang, J. C.; Frenkel, A. I.; Cuenya, B. R. *J. Am. Chem. Soc.* **2011**, *133*, 13455.
(36) Kongstein, O. E.; Bertocci, U.; Stafford, G. R. *J. Electrochem. Soc.* **2005**, *152*, C116.
(37) Shin, J. W.; Bertocci, U.; Stafford, G. R. *J. Phys. Chem. C* **2010**, *114*, 7926.
(38) Heaton, T.; Friesen, C. *J. Phys. Chem. C* **2007**, *111*, 14433.
(39) Seo, M.; Serizawa, Y. *J. Electrochem. Soc.* **2003**, *150*, E472.
(40) Lafouresse, M. C.; Bertocci, U.; Stafford, G. R. *J. Electrochem. Soc.* **2013**, *160*, H636.
(41) Lytle, F. W.; Wei, P. S. P.; Greegor, R. B.; Via, G. H.; Sinfelt, J. H. *J. Chem. Phys.* **1979**, *70*, 4849.
(42) Mansour, A. N.; Cook, J. W.; Sayers, D. E. *J. Phys. Chem.* **1984**, *88*, 2330.
(43) Croze, V.; Ettingshausen, F.; Melke, J.; Soehn, M.; Stuermer, D.; Roth, C. *J. Appl. Electrochem.* **2010**, *40*, 877.
(44) Mathew, R. J.; Russell, A. E. *Top. Catal.* **2000**, *10*, 231.
(45) de Groot, F. *Chem. Rev. (Washington, DC, U. S.)* **2001**, *101*, 1779.
(46) Koningsberger, D. C.; Mojet, B. L.; van Dorssen, G. E.; Ramaker, D. E. *Top. Catal.* **2000**, *10*, 143.
(47) Frenkel, A. I.; Small, M. W.; Smith, J. G.; Nuzzo, R. G.; Kvashnina, K. O.; Tromp, M. *J. Phys. Chem. C* **2013**, *117*, 23286.
(48) Small, M. W.; Kas, J. J.; Kvashnina, K. O.; Rehr, J. J.; Nuzzo, R. G.; Tromp, M.; Frenkel, A. I. *ChemPhysChem* **2014**, DOI: 10.1002/cphc.201400055.
(49) Kongkanand, A.; Ziegelbauer, J. M. *J. Phys. Chem. C* **2012**, *116*, 3684.
(50) Myers, V. S.; Frenkel, A. I.; Crooks, R. M. *Langmuir* **2012**, *28*, 1596.
(51) Erickson, E. M.; Thorum, M. S.; Vasić, R.; Marinković, N. S.; Frenkel, A. I.; Gewirth, A. A.; Nuzzo, R. G. *J. Am. Chem. Soc.* **2012**, *134*, 197.
(52) Zhang, X.; Cahill, D. G. *Langmuir* **2006**, *22*, 9062.
(53) Zhang, X.; Cahill, D. G.; Coronell, O.; Mariñas, B. J. *J. Membr. Sci.* **2009**, *331*, 143.
(54) Langer, J. L.; Economy, J.; Cahill, D. G. *Macromolecules* **2012**, *45*, 3205.
(55) Korobko, R.; Patlolla, A.; Kossoy, A.; Wachtel, E.; Tuller, H. L.; Frenkel, A. I.; Lubomirsky, I. *Adv. Mater. (Weinheim, Ger.)* **2012**, *24*, 5857.
(56) Stoney, G. G. *Proc. R. Soc. London, Ser. A* **1909**, *82*, 172.
(57) Stamenković, V.; Schmidt, T. J.; Ross, P. N.; Marković, N. M. *J. Electroanal. Chem.* **2003**, *554*−*555*, 191.
(58) Newville, M. *J. Synchrotron Radiat.* **2001**, *8*, 322.
(59) Ravel, B.; Newville, M. *J. Synchrotron Radiat.* **2005**, *12*, 537.
(60) Zabinsky, S. I.; Rehr, J. J.; Ankudinov, A.; Albers, R. C.; Eller, M. J. *Phys. Rev. B* **1995**, *52*, 2995.
(61) Santos, M. C.; Miwa, D. W.; Machado, S. A. S. *Electrochem. Commun.* **2000**, *2*, 692.
(62) Srejić, I.; Smiljanić, M.; Rakočević, Z.; Štrbac, S. *Int. J. Electrochem. Sci.* **2011**, *6*, 3344.
(63) Sitta, E.; Varela, H. *J. Solid State Electrochem* **2008**, *12*, 559.
(64) Tavassol, H.; Chan, M. K. Y.; Catarello, M. G.; Greeley, J.; Cahill, D. G.; Gewirth, A. A. *J. Electrochem. Soc.* **2013**, *160*, A888.
(65) Haiss, W. *Rep. Prog. Phys.* **2001**, *64*, 591.
(66) Feibelman, P. J. *Phys. Rev. B* **1997**, *56*, 2175.
(67) Frenkel, A. I.; Hills, C. W.; Nuzzo, R. G. *J. Phys. Chem. B* **2001**, *105*, 12689.
(68) Frenkel, A. I. *J. Synchrotron Radiat.* **1999**, *6*, 293.
(69) Wang, L.-L.; Johnson, D. D. *J. Am. Chem. Soc.* **2007**, *129*, 3658.
(70) Brako, R.; Sokcevic, D. *Surf. Sci.* **2000**, *469*, 185.
(71) Sakong, S.; Gross, A. *Surf. Sci.* **2003**, *525*, 107.
(72) Schwennicke, C.; Jurgens, D.; Held, G.; Pfnur, H. *Surf. Sci.* **1994**, *316*, 81.
(73) Zasada, I.; Van Hove, M. A. *Surf. Sci.* **2000**, *457*, L421.
(74) Starke, U.; Barbieri, A.; Materer, N.; Vanhove, M. A.; Somorjai, G. A. *Surf. Sci.* **1993**, *286*, 1.
(75) Wang, J. X.; Robinson, I. K.; Ocko, B. M.; Adzic, R. R. *J. Phys. Chem. B* **2005**, *109*, 24.
(76) Hyman, M. P.; Medlin, J. W. *J. Phys. Chem. C* **2007**, *111*, 17052.
(77) Roldan Cuenya, B.; Alcántara Ortigoza, M.; Ono, L. K.; Behafarid, F.; Mostafa, S.; Croy, J. R.; Paredis, K.; Shafai, G.; Rahman, T. S.; Li, L.; Zhang, Z.; Yang, J. C. *Phys. Rev. B* **2011**, *84*, 245438.
(78) Sanchez, S. I.; Menard, L. D.; Bram, A.; Kang, J. H.; Small, M. W.; Nuzzo, R. G.; Frenkel, A. I. *J. Am. Chem. Soc.* **2009**, *131*, 7040.
(79) Swain, M. V.; Menčík, J. *Thin Solid Films* **1994**, *253*, 204.
(80) Salvadori, M. C.; Brown, I. G.; Vaz, A. R.; Melo, L. L.; Cattani, M. *Phys. Rev. B* **2003**, *67*, 153404.
(81) In *CRC Handbook of Engineering Tables*; CRC Press: Boca Raton, FL, 2003; p 3.